Int J Adv Manuf Technol (2015) 78:1641–1649
DOI 10.1007/s00170-014-6768-5

ORIGINAL ARTICLE

FEM analysis on the abrasive erosion process in ultrasonic-assisted abrasive waterjet machining

Zhe Lv · Chuanzhen Huang · Hongtao Zhu · Jun Wang · Peng Yao · Zengwen Liu

Received: 10 May 2014 / Accepted: 29 December 2014 / Published online: 13 January 2015

Abstract In this work, a finite element method (FEM) explicit dynamic simulation was employed to investigate the abrasive erosion process in ultrasonic-assisted abrasive waterjet (AWJ) machining. Johnson-Holmquist ceramic material model with failure criteria was utilized to realize the deletion of the failure elements for the simulation of material removal. The effects of impact angle and particle shape on the erosion rate were analyzed. The residual stress in workpiece induced by the erosion under the vibration condition was compared to that under the non-vibration condition. Furthermore, the ultrasonic-assisted erosion processes of multiple particles under different overlapping conditions on the impact areas were simulated. The simulation results show that the application of vibration can effectively improve the erosion rate and influences the contact process between the particle and the workpiece surface. The residual stress distribution in the section of workpiece parallel to the vibration direction is not symmetric under the vibration condition, which is quite different from the nearly symmetric one obtained without vibration.

Keywords FEM · Abrasive waterjet · Ultrasonic machining · Erosion

Z. Lv · C. Huang (✉) · H. Zhu · J. Wang · P. Yao · Z. Liu
Center for Advanced Jet Engineering Technologies (CaJET), Key Laboratory of High-efficiency and Clean Mechanical Manufacture (Ministry of Education), School of Mechanical Engineering, Shandong University, Jinan 250061, China
e-mail: huangcz7@163.com

1 Introduction

Abrasive waterjet (AWJ) machining is one of the fastest growing non-traditional machining methods. With this method, water is pumped to a high pressure and then ejected through a sapphire orifice to form a high-velocity jet. As it goes into a mixing chamber, abrasive particles, such as garnet, alumina, silicon carbide, etc., are added into the jet. The momentum of the water is transferred to the particles inside the mixing chamber and the focusing nozzle, so that the abrasive particles attain sufficient energy for material removal [1]. In order to fulfill the requirements of reducing surface damage and ensuring processing accuracy, a low pressure and fine abrasives are implemented in AWJ [2], and thus, the processing efficiency was relatively low.

With the development of non-traditional machining, ultrasonic vibration is widely applied in turning, grinding, electric discharge machining (EDM), and polishing so as to enhance the processing efficiency and quality [3–6]. Tawakoli [7] found that the grinding force had a reduction of 70 % and the grinding efficiency was obviously improved by applying ultrasonic vibration on the workpiece and the thermal damage was significantly reduced. Nik [8] compared the experimental results of the conventional grinding (CG) with ultrasonic vibration-assisted grinding (UAG) and found that the surface quality and machining efficiency had a considerable improvement by using UAG. Mulik [9] applied the ultrasonic vibration on the workpiece to assist the magnetic abrasive finishing. The results demonstrated that the normal force was lower and the cutting torque was greater compared to traditional magnetic abrasive finishing and thus, the material removal rate was increased. Therefore, it is a promising way to improve the

processing efficiency by applying ultrasonic vibration on the workpiece in AWJ machining.

Many researchers have used finite element method (FEM) to simulate the solid particle erosion process occurred in abrasive machining [10–14]. Woytowiyz [15] simulated the impact of multiple spherical particles with a 3D FEM model and predicted the erosion rates by computing average damage and extrapolating to the level of 1.0. The results were in good agreement with the published experimental results. Eltobgy [16] used FEM to simulate the particle erosion process using an elasto-plastic material model with failure criteria. The variation of erosion rate with particle velocity and impact angle was coincident with the results obtained by both analytical and experimental methods. He also analyzed the residual stress generated during the erosion process and found that the profile was similar to that observed in shot peening process. Junkar [17] analyzed the influences of AWJ parameters on the geometric characteristics of the erosion craters by using an explicit FEM and verified the results by conducting corresponding experiments.

In this work, the abrasive erosion process in ultrasonic vibration-assisted AWJ machining was analyzed by using an FEM explicit dynamic code. The effects of different process parameters including impact angle and particle shape were investigated by adjusting the simulation model. Erosion rates under both vibration and non-vibration conditions were calculated to discuss the effect of the vibration on the erosion efficiency. The contact force histories and velocity histories of the particles were acquired to illustrate the influence of the workpiece vibration on the erosion process. The residual stress distributions at the impact zones under vibration and non-vibration conditions were compared. Moreover, the erosion process by multiple particles in ultrasonic vibration-assisted AWJ was also simulated.

2 Simulation procedure

2.1 Explicit dynamics

Due to the high speed and small dimension of the eroding particle, the impact process takes a quite short time and will cause a high strain rate in the target material. These issues will lead to convergence problem and numerical instabilities in analyzing by using implicit methods [17]. Thus an explicit dynamic FEM code LS-DYNA was applied to conduct the simulation.

Table 1 Johnson-Holmquist ceramics model parameters for AlN

Parameters	Values
Density (kg/m^3)	3226
Shear modulus (GPa)	127
A	0.85
B	0.31
C	0.013
M	0.21
N	0.29
EPSI	1.0
Tensile strength (GPa)	0.32
HEL (GPa)	9
HEL pressure (GPa)	5
HEL bulk strain (GPa)	0.0242
HEL strength (GPa)	6
D1	0.02
D2	1.85
K1 (GPa)	201
K2 (GPa)	260
K3 (GPa)	0
Beta	1.0

Updated Lagrangian formulation of the governing equation is utilized in LS-DYNA solver. The discrete form of the motion equations at time n is [18]

$$Ma_n = P_n - F_n + H_n \tag{1}$$

Where M is the mass matrix, a is the acceleration, P is the external force, F is the stress divergence vector, and H is the hourglass resistance.

Using central difference time integration, the nodal velocity u_{n+1} at time $n+1$ can be calculated as follows:

$$v_{n+1/2} = v_{n-1/2} + a_n \Delta t_n \tag{2}$$

$$u_{n+1} = u_n + v_{n+1/2}(\Delta t_n + \Delta t_{n+1})/2 \tag{3}$$

Then, u_{n+1} is substituted into the geometric equation and physical equation to acquire the strain and stress at time $n+1$.

Table 2 Properties of the abrasive

Material	Composition (%)		Density (g/cm^3)	Mohs hardness
	SiC	Fe_2O_3		
SiC	>97.5	<0.7	3.2	>9

The central difference is stabilized only when the time step is lower than a critical value. For solid elements, this critical value Δt_{cr} can be expressed as [18]

$$\Delta t_{cr} = \frac{L_e}{Q + \left(Q^2 + c^2\right)^{1/2}} \tag{4}$$

where L_e is a characteristic length of the element, c is the sound speed in the solid material, and Q is a function of the bulk viscosity coefficients.

2.2 Material model

The workpiece material used in simulation was aluminum nitride, and Johnson-Holmquist ceramics (JH-2) model was employed to model the workpiece material. The constants in JH-2 model for AlN are listed in Table 1 [19]. Silicon carbide was employed as the abrasive powders and hard to break during the impact [20]. For simplification, it was modeled as a rigid body in simulation with its properties listed in Table 2.

Johnson-Holmquist ceramics model is applicable for brittle materials subjected to large strains, high strain rates, and high pressures [21]. The strength and pressure parameters in JH-2 model are normalized by the corresponding components at Hugoniot elastic limit (HEL) for the sake of comparison between different materials. The normalized equivalent stress is

$$\sigma^* = \sigma^*_i - D\left(\sigma^*_i - \sigma^*_f\right) \tag{5}$$

where σ^*_i is the normalized intact equivalent stress, σ^*_f is the normalized fracture stress and D is the damage ($0 \le D \le 1$). σ^*, σ^*_i, and σ^*_f have the general form $\sigma^* = \sigma/\sigma_{\mathrm{HEL}}$. The normalized intact strength is given by

$$\sigma^*_i = A(P^* + T^*)^N \left(1 + C \cdot \ln \dot{\varepsilon}^*\right) \tag{6}$$

and the normalized fracture strength is given by

$$\sigma^*_f = B(P^*)^M \left(1 + C \cdot \ln \dot{\varepsilon}^*\right) \tag{7}$$

where $P^* = P/P_{\mathrm{HEL}}$ and $T^* = T/P_{\mathrm{HEL}}$ and P and T are the hydrostatic pressure and maximum tensile pressure which the material can withstand, respectively. P_{HEL} is the pressure at HEL. A, B, C, M, and N are material constants. $\dot{\varepsilon}^* = \dot{\varepsilon}/\dot{\varepsilon}_0$, where $\dot{\varepsilon}$ is the strain rate and $\dot{\varepsilon}_0 = 1 s^{-1}$.

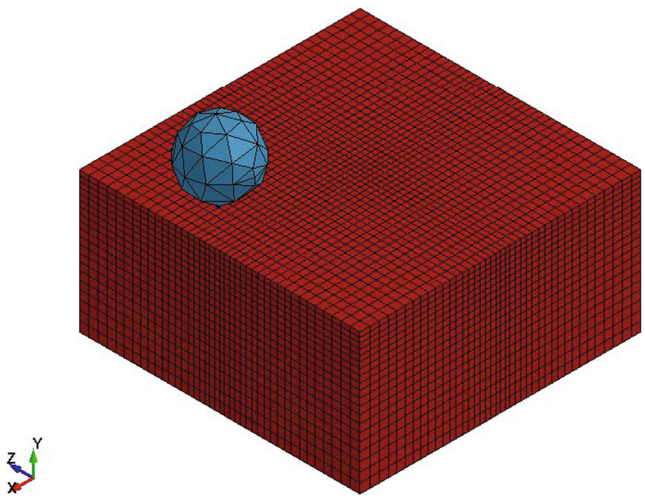

Fig. 1 Meshed model of the particle and the workpiece

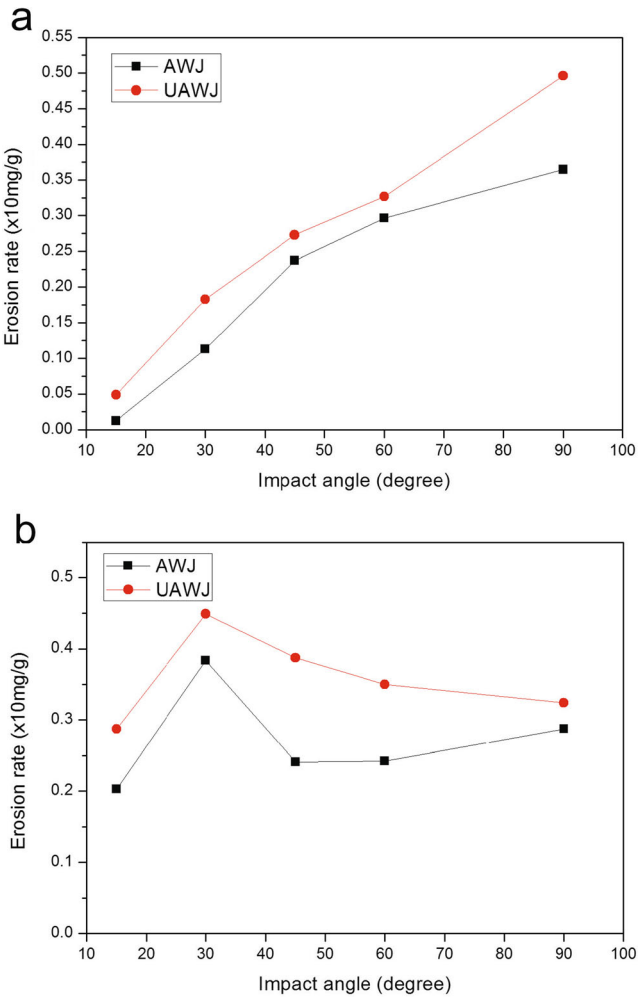

Fig. 2 Erosion rate under different process parameters (**a** blunt particles; **b** sharp particles)

The strength of the hard brittle materials under dynamic loading is strongly influenced by the hydrostatic pressure. From the equation of state for the material, the hydrostatic pressure P can be expressed as

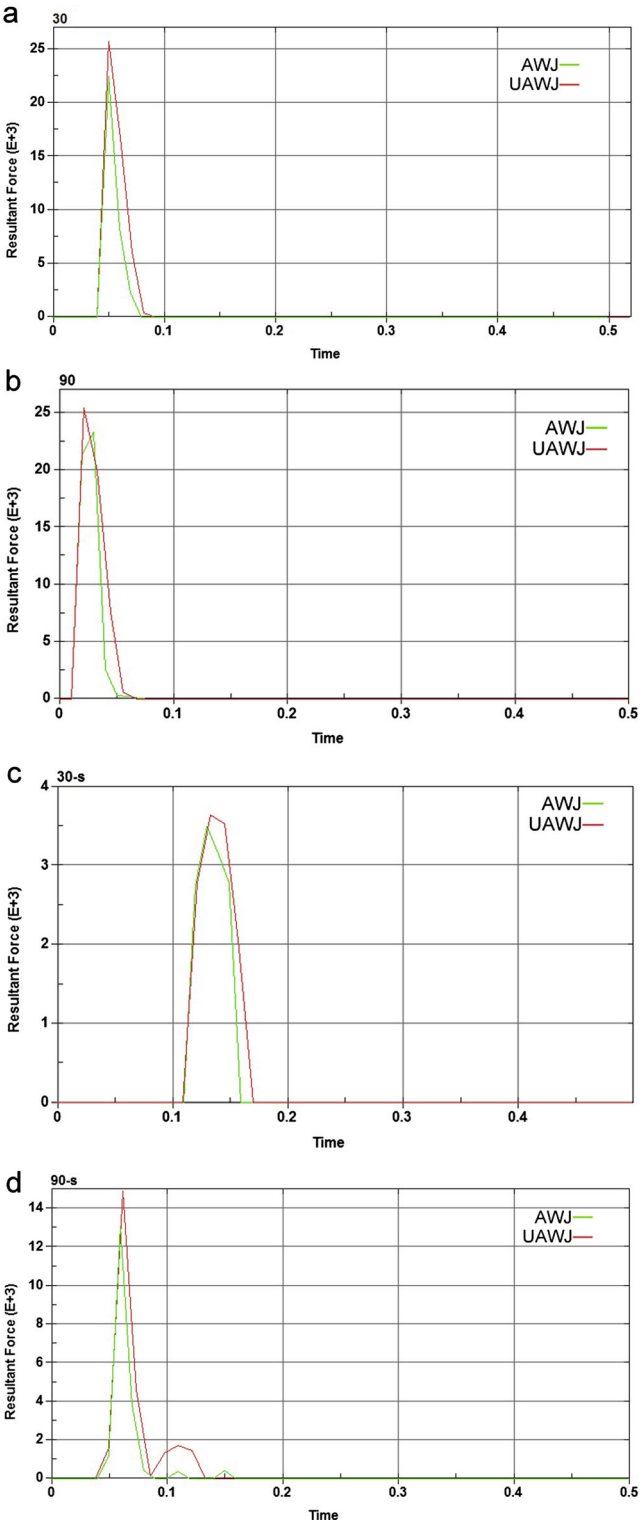

Fig. 3 Contact force histories under different conditions (**a** impact angle 30°, blunt particle; **b** impact angle 90°, blunt particle; **c** impact angle 30°, sharp particle; **d** impact angle 90°, sharp particle)

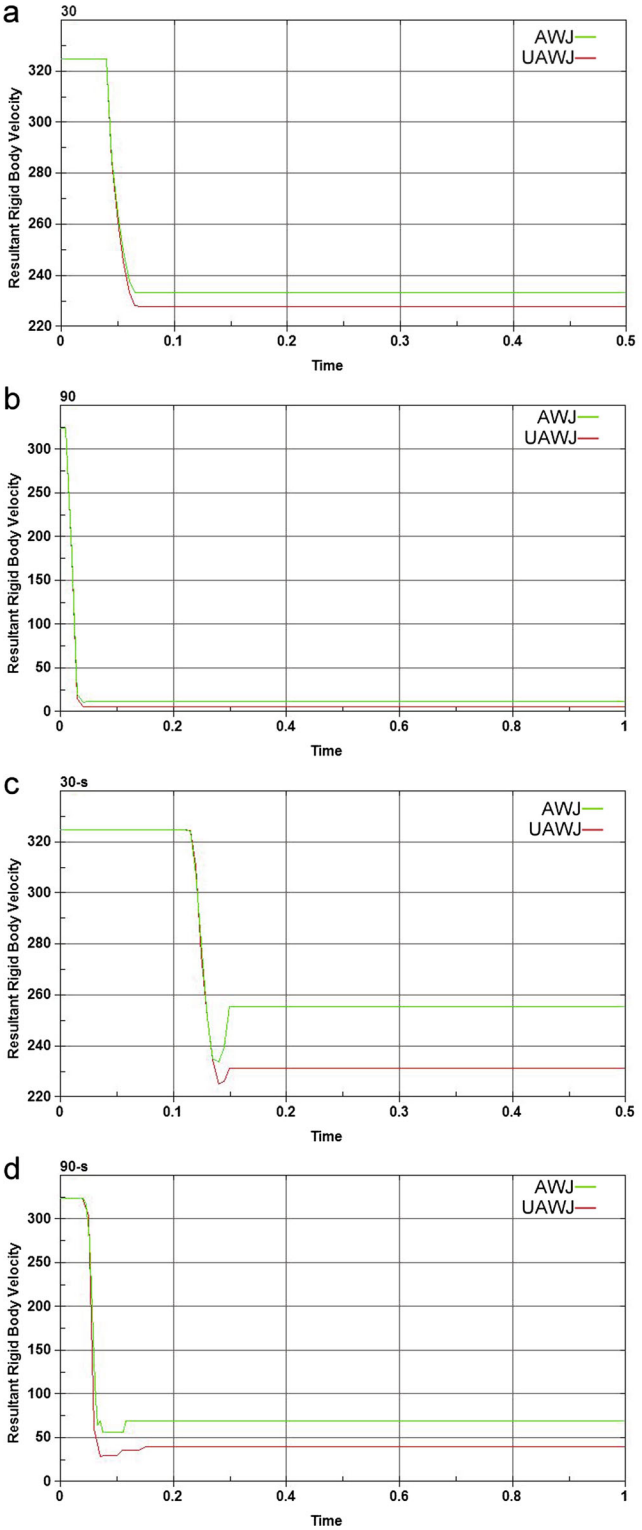

Fig. 4 Velocity history of the particles under different process parameters (**a** impact angle 30°, blunt particle; **b** impact angle 90°, blunt particle; **c** impact angle 30°, sharp particle; **d** impact angle 90°, sharp particle)

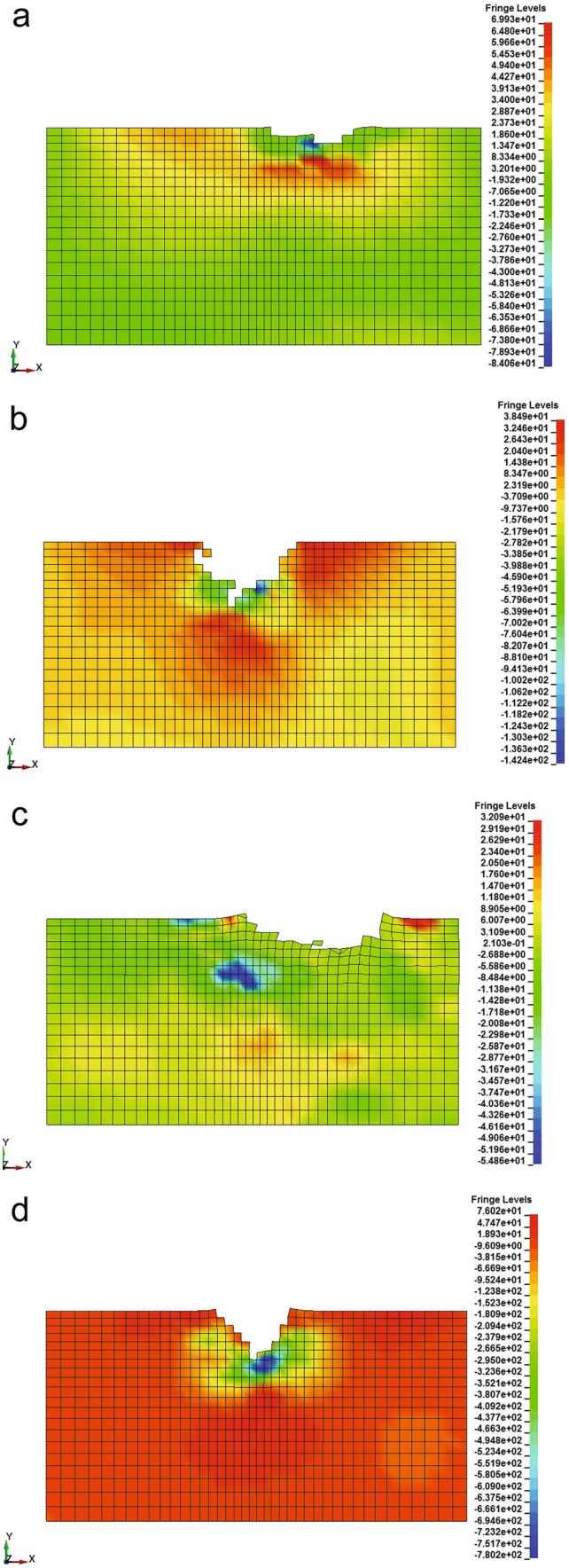

Fig. 5 Residual stress in the longitudinal section (**a** impact angle 30°, blunt particle; **b** impact angle 90°, blunt particle; **c** impact angle 30°, sharp particle; **d** impact angle 90°, sharp particle)

$$P = K_1 \cdot \mu + K_2 \cdot \mu^2 + K_3 \cdot \mu^3 + \Delta P \tag{8}$$

where K_1, K_2, and K_3 are constants, $\mu = \rho/\rho_0 - 1$, ρ is the current density, and ρ_0 is the initial density. ΔP is the incremental pressure due to the damage accumulation.

The damage D is expressed as

$$D = \Sigma \Delta \varepsilon^P / \varepsilon_f^P \tag{9}$$

where $\Delta \varepsilon^P$ is the plastic strain increment and ε_f^P is the plastic strain to fracture under a constant pressure:

$$\varepsilon_f^P = D_1 (P^* + T^*)^{D_2} \tag{10}$$

where D_1 and D_2 are material constants.

2.3 Model and boundary conditions

The workpiece was modeled as a cuboid and meshed using the eight-node brick hexahedral elements with one integration point (solid 164), and the particle was meshed using the four-node tetrahedral elements. The size of the workpiece model is 40 μm×40 μm×20 μm. The meshed model is shown in Fig. 1. The block surfaces were set as non-reflecting boundaries except the upper surface which is impacted by the particle. The contact type was chosen as the surface to surface eroding regime between the particle and the workpiece for ensuring that the contact will continue after the failure of the surface elements. The static and dynamic coefficients of friction were set as 0.2 and 0.15, respectively [16].

The period of the workpiece vibration is 50 μs when using 20-kHz exciting frequency. In erosion process, the time duration of the abrasive particle contacting with the workpiece surface is less than 0.1 μs in preliminary simulation test, which is much less than the vibration period. Thus, it can be approximated that the velocity of the workpiece keeps as a constant during the contact process. The magnitude of the average vibration velocity of workpiece can be calculated as [7]

$$v_f = f \int_0^{1/f} 2\pi f A \cos 2\pi f \, dt \tag{11}$$

A curve of vibration velocity versus the time can be defined with this velocity value. The direction of the vibration velocity is perpendicular to the impact velocity of the particle. The beginning and the ending time of the curve depends on the eroding condition. In order to simulate the workpiece

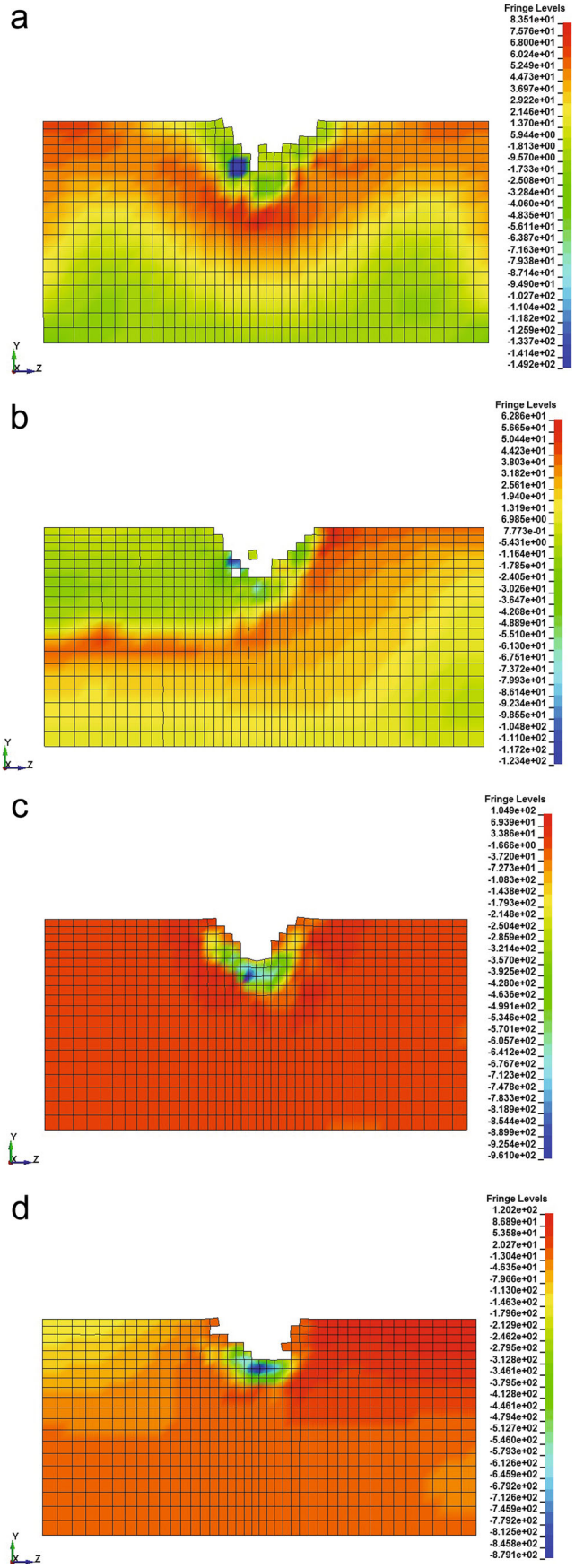

Fig. 6 Residual stress in the cross-section parallel to the vibration direction under the impact angle of 90° (**a** non-vibration, blunt particle; **b** vibration, blunt particle; **c** non-vibration, sharp particle; **d** vibration, sharp particle.)

vibration in the ultrasonic-assisted AWJ machining, the time-dependent load defined by the curve was applied to the nodes on boundary surfaces of the target model normal to z axis. The degrees of freedom along z axis of the nodes under the loading were coupled. One thing to note here is that under the loading condition, only the degrees of freedom along x axis and y axis of the nodes on the bottom surface of the workpiece were constrained.

The abrasive particles used in AWJ can be categorized as blunt and sharp ones [22]. Thus, the particles are modeled as sphere and octahedron in order to substitute the blunt and the sharp particle, respectively. The diameter of the sphere is 10 μm and the octahedron has the volume equal to the sphere. The impact angles ranges from 15 to 90° with an increment of 15°.

3 Results and discussion

3.1 Erosion rate

After the calculation, the number of elements deleted from the model due to failure was counted and the erosion rate was calculated. The erosion rate used to characterize the erosion performance of the target material is defined as

$$\text{erosion rate} = \frac{\text{mass of deleted workpiece elements}}{\text{mass of impact particles}} \quad (12)$$

Figure 2 shows the variation of the erosion rate with the impact angle under different process parameters. It can be seen that the erosion rate increases with an increase in the impact angle and reaches the maximum at the impact angle of 90° using blunt particles, which is similar as the trend of the variation of erosion rate versus the impact angle found by Bitter [23] in the erosion tests of annealed glass. However, the erosion rate reaches the maximum at the impact angle of 30° when using sharp particles, showing an obvious feature of micro-cutting mechanism. The trend is similar to that obtained from the erosion tests performed by Finnie [24], which suggests that micro-cutting mechanism is dominant in the material removal.

For two types of particle shapes, the erosion rates under the vibration conditions are always higher than those under the non-vibration conditions, demonstrating that the application of workpiece vibration can effectively improve the material removal efficiency. This is caused by the dynamics variation

of the erosion process including the enhanced impact load and the extended scratching length [8].

3.2 Contact force history

The histories of the contact force between the particle and workpiece surface were obtained by the simulation and shown in Fig. 3. It can be found that the contact force magnitudes under the vibration conditions are higher than those under the non-vibration conditions. This is because that the vibration enhanced the impact load between the particle and workpiece surface. Also, the duration time of the contact is a bit longer when applying vibration. The improvements in contact force and contact duration time are contributive to increase the material removal rate during the erosion process.

3.3 Particle velocity history

During the erosion process, the kinetic energy of the particle is mainly dissipated by the deformation and removal of the workpiece materials. Thus, the velocity of the particle will undergo a severe reduction. Figure 4 shows the time histories of particle velocity under different process parameters. Compared with the velocity under the non-vibration condition, the velocity under the vibration condition decreases severely, indicating that a larger amount of energy is consumed in removing the workpiece material.

3.4 Residual stress

Figure 5 shows the simulation results of the residual stress on the workpiece induced by the particle erosion. It can be seen from Fig. 5a that the compressive stress exists right below the crater. The stress changes to be tensile with an increase in the depth along the y axis and reaches a maximum at a few micrometers below the crater. In addition, the tensile stress appears in front of the crater, which is caused by the deformation of the workpiece material due to the scratching by the particle. In Fig. 5b, the compressive stress exists at the immediate vicinity below the lowest point of the crater and tends to be tensile with an increase in the depth along the y axis, which is similar to the trend of the residual stress by shot peening over the depth measured by Wang [25]. The periphery of the crater is characterized by tensile stress. The stress distribution is almost symmetric. Hong [26] acquired a similar residual stress distribution in the simulation of single shot impacting. The domain size of the residual stress at the impact angle of 90° is larger than that at the impact angle of 30°. It can be seen from Fig. 5c that the residual stress distribution caused by the sharp particle is quite different from that generated by the blunt particle. The domain size of the compressive stress is obviously larger than that generated by the blunt particle. Also, the position of the tensile stress zone is lower. The stress distribution caused by the sharp particle at the impact angle of 90°, as shown in Fig. 5d, is similar to that caused by the blunt particle except that the size of the compressive stress is larger.

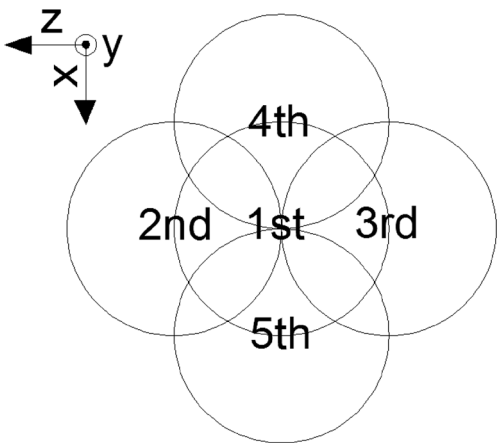

Fig. 7 Illustration of the relative locations of five particles' projections on the impact area under partially overlapping condition

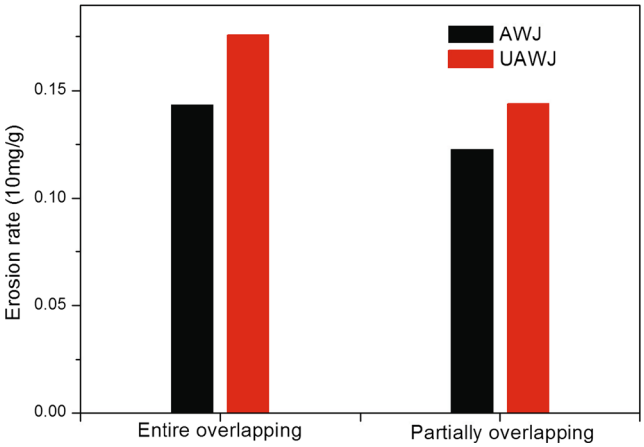

Fig. 8 Erosion rate under different overlapping conditions

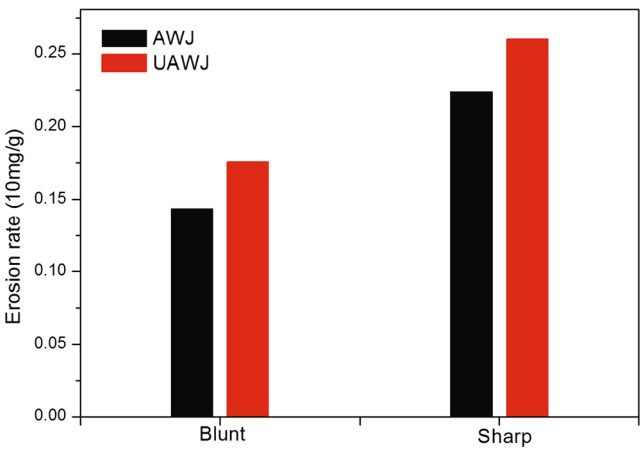

Fig. 9 Erosion rate under different particle shapes

Figure 6 shows the differences of the residual stress distributions between the ones obtained with and without the workpiece vibration. It can be found that the stress distributions in Fig. 6b, d, obtained using workpiece vibration by blunt particle and sharp particle, respectively, are not symmetric, which are quite different from the nearly symmetric ones obtained with no vibration as shown in Fig. 6a, c.

3.5 Multi-particle erosion simulation

Different situations were carried out to analyze the erosion effect of the multi particles. The number of the particles was five and the impact angle was 30°. Particles impacting the same point and impacting the different points with certain distances (as shown in Fig. 7) were modeled to investigate the effect of the overlapping conditions in the impact areas. Also, the effect of the particle shape was considered.

Figures 8 and 9 are the erosion rates of multiple particles under different conditions. It can be seen from Fig. 8 that the erosion rates under partially overlapping conditions are lower than those under entire-overlapping conditions. Also, the sharp particle can cause higher erosion rate at the impact angle of 30°. For all conditions, the erosion rates with the workpiece vibration are higher than those without vibration.

Figure 10 shows the residual stress at the impact area induced by the erosion of multiple particles. It can be found from Fig. 10a that the domain size of the tensile residual stress below the crater under entire-overlapping condition is very large. However, the compressive stress is dominant below the erosion crater under partially overlapping condition as shown in Fig. 10b. The compressive stress generated by erosion can increase the fatigue strength of the workpiece surface, which is preferred in surface machining [25].

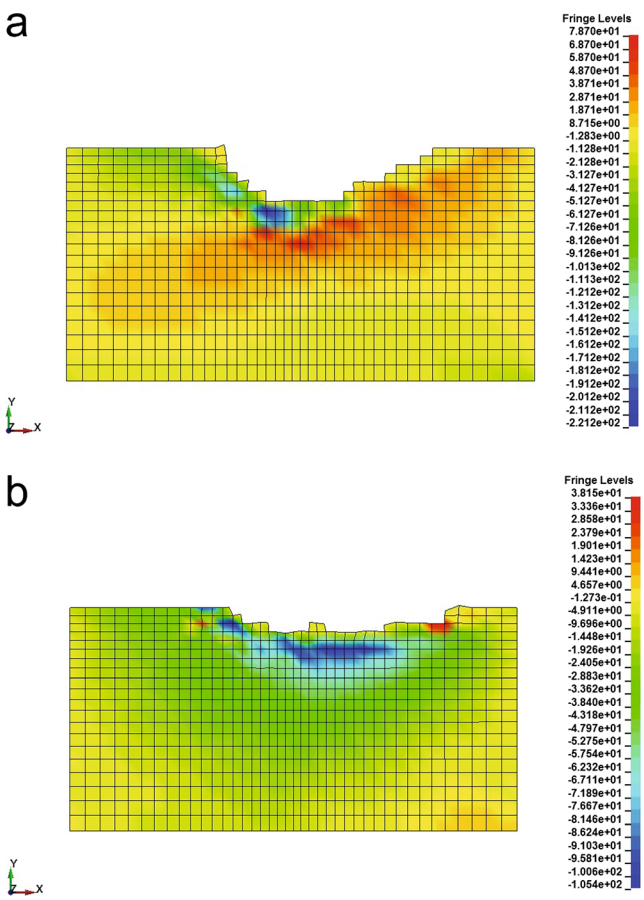

Fig. 10 The residual stress of the section under different overlapping conditions (**a** entire overlapping; **b** partially overlapping)

4 Conclusions

An explicit dynamic FEM analysis was conducted to investigate the erosion process in ultrasonic-assisted AWJ machining. Simulation results show that the maximum erosion rate of the blunt particles is acquired at the impact angle of 90°. However, the maximum erosion rate of the sharp particles is acquired at the impact angle of 30°, demonstrating an obvious micro-cutting mechanism of material removal. For both particle shapes, the erosion rates under the vibration conditions are always higher than those under the non-vibration conditions, demonstrating that the application of workpiece vibration can effectively improve the machining efficiency of AWJ. The contact force magnitudes under the vibration conditions are higher than those under the non-vibration conditions. Also, the duration time of the contact is increased when the vibration is applied. The velocity loss of the particle during erosion process is severe under the vibration condition, indicating that a larger amount of energy is consumed in removing the workpiece material. The residual stress distribution in the section of workpiece parallel to the vibration direction is not symmetric under the vibration condition, which is quite different from the nearly symmetric one obtained without vibration. The erosion process of multiple particles was also simulated. The results show that the erosion rates under partially overlapping conditions are lower than those under entire-overlapping conditions. The compressive residual stress is generated after the erosion under partially overlapping condition, which is preferred in precision surface machining.

Acknowledgments This work is supported by National Natural Science Foundation of China (51175307, 51375273).

References

1. Paul S, Hoogstrate AM, van Luttervelt CA, Kals HJJ (1998) Analytical modelling of the total depth of cut in the abrasive water jet machining of polycrystalline brittle material. J Mater Process Technol 73:206–212. doi:10.1016/S0924-0136(97)00230-6
2. Zhu HT, Huang CZ, Wang J, Li QL, Che CL (2009) Experimental study on abrasive waterjet polishing for hard–brittle materials. Int J Mach Tools Manuf 49:569–578. doi:10.1016/j.ijmachtools.2009.02.005
3. Nategh MJ, Razavi H, Abdullah A (2012) Analytical modeling and experimental investigation of ultrasonic-vibration assisted oblique turning, part I: kinematics analysis. Int J Mech Sci 63:1–11. doi:10.1016/j.ijmecsci.2012.04.007
4. Razavi H, Nategh MJ, Abdullah A (2012) Analytical modeling and experimental investigation of ultrasonic-vibration assisted oblique turning, part II: dynamics analysis. Int J Mech Sci 63:12–25. doi:10.1016/j.ijmecsci.2012.05.005
5. Razavi H, Nategh MJ, Abdullah A (2012) Analytical modeling and experimental investigation of ultrasonic-vibration assisted oblique turning, part III: experimental investigation. Int J Mech Sci 63:26–36. doi:10.1016/j.ijmecsci.2012.06.007
6. Uhlmann E, Spur G (1998) Surface formation in creep feed grinding of advanced ceramics with and without ultrasonic assistance. CIRP Ann Manuf Technol 47:249–252. doi:10.1016/S0007-8506(07)62828-5
7. Tawakoli T, Azarhoushang B (2008) Influence of ultrasonic vibrations on dry grinding of soft steel. Int J Mach Tools Manuf 48:1585–1591. doi:10.1016/j.ijmachtools.2008.05.010
8. Nik MG, Movahhedy MR, Akbari J (2012) Ultrasonic-assisted grinding of Ti6Al4V alloy. Procedia CIRP 1:353–358. doi:10.1016/j.procir.2012.04.063
9. Mulik RS, Pandey PM (2010) Mechanism of surface finishing in ultrasonic-assisted magnetic abrasive finishing process. Mater Manuf Process 25:1418–1427. doi:10.1080/10426914.2010.499580
10. Yu F, Wang JM, Liu FH (2011) Numerical simulation of single particle acceleration process by SPH coupled FEM for abrasive waterjet cutting. Int J Adv Manuf Technol 59:193–200. doi:10.1007/s00170-011-3495-z
11. Jayswal SC, Jain VK, Dixit PM (2005) Modeling and simulation of magnetic abrasive finishing process. Int J Adv Manuf Technol 26:477–490. doi:10.1007/s00170-004-2180-x
12. Kumar G, Yadav V (2008) Temperature distribution in the workpiece due to plane magnetic abrasive finishing using FEM. Int J Adv Manuf Technol 41:1051–1058. doi:10.1007/s00170-008-1557-7
13. Wang JM, Gao N, Gong WJ (2010) Abrasive waterjet machining simulation by SPH method. Int J Adv Manuf Technol 50:227–234. doi:10.1007/s00170-010-2521-x
14. Wang JM, Liu FH, Yu F, Zhang G (2011) Shot peening simulation based on SPH method. Int J Adv Manuf Technol 56:571–578. doi:10.1007/s00170-011-3193-x
15. Woytowitz P, Richman R (1999) Modeling of damage from multiple impacts by spherical particles. Wear 233–235:120–133. doi:10.1016/S0043-1648(99)00173-8
16. ElTobgy M, Ng E, Elbestawi M (2005) Finite element modeling of erosive wear. Int J Mach Tools Manuf 45:1337–1346. doi:10.1016/j.ijmachtools.2005.01.007
17. Junkar M, Jurisevic B, Fajdiga M, Grah M (2006) Finite element analysis of single-particle impact in abrasive water jet machining. Int J Impact Eng 32:1095–1112. doi:10.1016/j.ijimpeng.2004.09.006
18. John O (1998) LS-DYNA theoretical manual. Livermore Software Technology Corporation, California
19. Holmquist TJ, Templeton DW, Bishnoi KD (2001) Constitutive modeling of aluminum nitride for large strain, high-strain rate, and high-pressure applications. Int J Impact Eng 25:211–231. doi:10.1016/S0734-743X(00)00046-4
20. Li WY, Wang J, Zhu HT, Li HZ, Huang CZ (2013) On ultrahigh velocity micro-particle impact on steels—a single impact study. Wear 305:216–227. doi:10.1016/j.wear.2013.06.011
21. Johnson GR, Holmquist TJ (1994) An improved computational constitutive model for brittle materials. AIP Conf Proc 309:981–984. doi:10.1063/1.46199
22. Momber A, Kovacevic R (1998) Principles of abrasive water jet machining. doi: 10.1007/978-1-4471-1572-4
23. Bitter J (1963) A study of erosion phenomena part I. Wear 6:5–21. doi:10.1016/0043-1648(63)90003-6
24. Finnie I (1960) Erosion of surfaces by solid particles. Wear 3:87–103. doi:10.1016/0043-1648(60)90055-7
25. Wang S, Li Y, Yao M, Wang R (1998) Compressive residual stress introduced by shot peening. J Mater Process Technol 73:64–73. doi:10.1016/S0924-0136(97)00213-6
26. Hong T, Ooi JY, Shaw B (2008) A numerical simulation to relate the shot peening parameters to the induced residual stresses. Eng Fail Anal 15:1097–1110. doi:10.1016/j.engfailanal.2007.11.017